metals

MDPI

Article

An Analysis of Dynamic Recrystallization During the Reduction Pretreatment Process Using a Multiscale Model

Die Wu [1,2], Zhen Ning [1,2], Yanlin Zhu [2] and Wei Yu [1,*]

[1] National Engineering Research Center of Flat Rolling Equipment, University of Science and Technology Beijing, Beijing 100083, China; 17778606018@163.com (D.W.); zhenning410@163.com (Z.N.)
[2] Institute for Mathematical and Computational Materials Science, Chengdu Advanced Metal Materials Industry Technology Research Institute Co., Ltd., Chengdu 610300, China; ali.yanlinzhu@outlook.com
* Correspondence: yuwei@nercar.ustb.edu.cn; Tel.: +86-13001183873

Abstract: In this study, a multiscale model is developed through secondary development (UMAT and UEXTERNALDB) in Abaqus with the objective of simulating the thermal deformation process with dynamic recrystallization behavior. The model couples the finite element method (FEM) with the multiphase field model (MPFM), thereby establishing bidirectional coupling between macroscopic mechanical behavior and microstructural evolution. A comparison between the single-element hot compression simulation and experimental results demonstrates that the model accurately simulates both the macroscopic mechanical behavior and microstructural evolution during the thermal deformation process, thereby exhibiting high precision. Simulations of the reduction pretreatment (RP) process under different reduction amounts and billet surface temperatures demonstrate that increasing the reduction amount and billet surface temperature significantly enhances both plastic deformation and the volume fraction of dynamic recrystallization in the billet core. This results in the closure of core voids and the refinement of the core microstructure, thereby providing valuable guidance for the development of optimal reduction pretreatment (RP) processes.

Keywords: multiscale model; finite element model; multiphase field model; reduction pretreatment process; dynamic recrystallization

check for updates

Citation: Wu, D.; Ning, Z.; Zhu, Y.; Yu, W. An Analysis of Dynamic Recrystallization During the Reduction Pretreatment Process Using a Multiscale Model. *Metals* **2024**, *14*, 1290. https://doi.org/10.3390/met14111290

Academic Editor: Srecko Stopic

Received: 27 September 2024
Revised: 4 November 2024
Accepted: 12 November 2024
Published: 14 November 2024

1. Introduction

To improve billet quality, researchers have developed the reduction pretreatment (RP) process [1–3]. This process utilizes the temperature gradient between the surface and the core of the billet, significantly reducing core defects and achieving excellent results in practical applications [2,3]. Current research primarily focuses on the effect of the RP process in enhancing the macroscopic performance of billets [4,5], while studies on its influence on microstructural evolution are relatively limited. Most existing studies rely on empirical models or finite element simulations based on experimental data [6–9], often overlooking the complex interactions between dynamic recrystallization and macroscopic mechanical behavior. This limits the comprehensive understanding of microstructural evolution. Additionally, current research on the improvement mechanism of the RP process remains mostly at the macroscopic level [1,3] and lacks in-depth explanations from the perspective of microstructural evolution. Due to the high costs, lengthy duration, and difficulty in controlling conditions during experimental studies of the RP process, computer simulations provide a more effective approach to analyzing the impact of process parameters on microstructural evolution.

Finite element models are frequently employed to simulate macroscopic mechanical behavior with considerations for dynamic recrystallization. Researchers often represent microstructural evolution through dynamic recrystallization volume fraction and average grain size, integrating these variables into material constitutive equations [10–12]. However, this approach faces several challenges. Firstly, the values for dynamic recrystallization volume fraction and average grain size are influenced by plastic deformation and temperature variations during thermal deformation. Accurately modeling these complex changes in deformation and temperature proves challenging [13–16]. Despite extensive research on dynamic recrystallization models based on uniaxial thermal compression experiments, there is limited application of these models to simulate actual thermal deformation processes. Additionally, this method fails to simulate the microstructure during thermal deformation.

Monte Carlo (MC) models [17–19], cellular automata (CA) models [20–23], and multiphase field (MPF) models [24,25] can simulate microstructural evolution during dynamic recrystallization and estimate the mechanical properties of materials. However, these models are typically only applicable to simple, uniform deformation. Real thermal deformation processes involve complex, inhomogeneous deformation that single mesoscopic models cannot adequately address (e.g., hot rolling, hot extrusion, and hot drawing).

To address this, researchers have increasingly adopted multiscale models. These models generally combine finite element models for macroscopic mechanical behavior with mesoscale models (such as Monte Carlo, cellular automata, or phase field models) for microstructural evolution [26–32]. A common approach involves performing finite element simulations first and then using the results as the initial conditions for the mesoscale model. However, these models use empirical constitutive equations that do not account for the impact of microstructural evolution on macroscopic mechanical behavior, leading to unidirectional coupling. In reality, dynamic recrystallization significantly affects macroscopic mechanical behavior. Therefore, developing a bidirectional coupled multiscale model that considers interactions between macroscopic mechanical behavior and microstructural evolution is crucial for studying microstructural evolution during the thermal deformation of dynamically recrystallized materials.

Tomohiro Takaki and his team pioneered a bidirectionally coupled multiscale model based on this concept [33,34]. However, their model's finite element component requires custom programming, making it prohibitively expensive for widespread adoption. Additionally, their study was restricted to uniaxial compression simulations. Thus, there is an urgent need for a more accessible and cost-effective multiscale model to enhance the simulations of the RP process.

In this study, we conducted the secondary development of the commercial finite element software Abaqus 6.14, coupled the finite element model with the phase field model, established a multiscale model to simulate the thermal deformation process, and then used the multiscale model to numerically simulate the RP process. The goal of this study was to optimize the RP process parameters through a multiscale simulation method.

2. Model Development

2.1. Multiphase Field Model

In this study, we employed the multiphase field dynamic recrystallization model developed by Takaki et al. [24,25] to simulate microstructural evolution during thermal deformation. The equation governing the time evolution of the MPFM variables is expressed as follows:

$$\frac{\partial \phi_{\mathrm{i}}}{\partial t} = -\sum_{j=1}^{n} \frac{2M^{\phi}}{n} \left[\sum_{k=1}^{n} \left\{ \left(W_{ik} - W_{jk} \right) \phi_k + \frac{1}{2} \left(a_{ik}^2 - a_{jk}^2 \right) \nabla^2 \phi_k - \frac{8}{\pi} \sqrt{\phi_i \phi_j} \Delta E_{ij} \right\} \right] \quad (1)$$

where α_{ij}, W_{ij}, and M^{Φ} are constants related to the grain boundary thickness δ, grain boundary energy γ, and grain boundary mobility M, as shown below:

$$\alpha_{ij} = \frac{4}{\pi} \sqrt{\delta \gamma},\ W_{ij} = \frac{2\gamma}{\delta},\ M^{\phi} = \frac{\pi^2}{16\delta} M \quad (2)$$

where the grain boundary mobility, M, is related to the grain boundary diffusion coefficient and can be expressed as follows:

$$M = \frac{\delta b D_b}{\mathrm{k}T} = \frac{\delta b D_{0b}}{\mathrm{k}T} exp\left(-\frac{Q_b}{\mathrm{R}T}\right) \tag{3}$$

where D_{0b} is the grain boundary diffusion coefficient at 0 K, Q_b is the activation energy for grain boundary diffusion, b is the Bergner vector, and k is the Boltzmann constant.

In Equation (1), ΔE_{ij} is the difference in deformation storage energy between grains i and j, which can be denoted as follows:

$$\Delta E_{ij} = \alpha \mu b^2 \left(\rho_i - \rho_j\right) \tag{4}$$

where α is the dislocation interaction coefficient, μ is the shear modulus of the material, and ρ is the dislocation density within the grains. In this study, the Kocks–Mecking model is used to describe the change in dislocation density during the deformation process:

$$\frac{d\rho}{d\varepsilon} = k_1\sqrt{\rho} - k_2\rho \tag{5}$$

where ε is the equivalent strain, k_1 is the constant associated with work hardening, and k_2 is the softening parameter associated with dynamic recovery.

The relationship between the dislocation density and yield strength, σ_f, is

$$\sigma_f = \alpha \mu b \sqrt{\rho} \tag{6}$$

It has been shown that the nucleation rate of dynamic recrystallization is related to the strain rate and the deformation temperature; therefore, the nucleation rate formula used in this study is as follows [35,36]:

$$n_{DRX} = C\dot{\varepsilon}^m exp\left(-\frac{Q_a}{\mathrm{R}T}\right) \tag{7}$$

where C is the fitting constant, m is a constant related to the strain rate, and Q_{a} is the nucleation activation energy.

2.2. UMAT Subroutine

In this study, in order to simulate the material behavior during thermal deformation, we developed the UMAT and UEXTERNALDB subroutines based on Abaqus, and we coupled the multiphase field model (MPFM) with the finite element model (FEM) in a multiscale framework. The yield stress σ_f calculated by the MPFM is transferred to the UMAT subroutine through the UEXTERNALDB subroutine, which is used as the basis for calculating the strain increment and updating the stress state. The computational flow of the UMAT subroutine is shown in Figure 1.

To calculate the elastic response of the material, an elastic stiffness matrix is first defined as **C**. For an isotropic material, the elastic stiffness matrix is based on the shear modulus of the material, μ, and the Lamé constant, λ, which is expressed as

$$\mathbf{C} = \begin{pmatrix} 2\mu+\lambda & \lambda & \lambda & 0 \\ \lambda & 2\mu+\lambda & \lambda & 0 \\ \lambda & \lambda & 2\mu+\lambda & 0 \\ 0 & 0 & 0 & \mu \end{pmatrix} \tag{8}$$

where the Lamé constant λ and the shear modulus μ can be calculated from the modulus of elasticity E and Poisson's ratio v of the material. The expression for the Lamé constant is given by

$$\lambda = \frac{E}{(1+v)(1-2v)}v \tag{9}$$

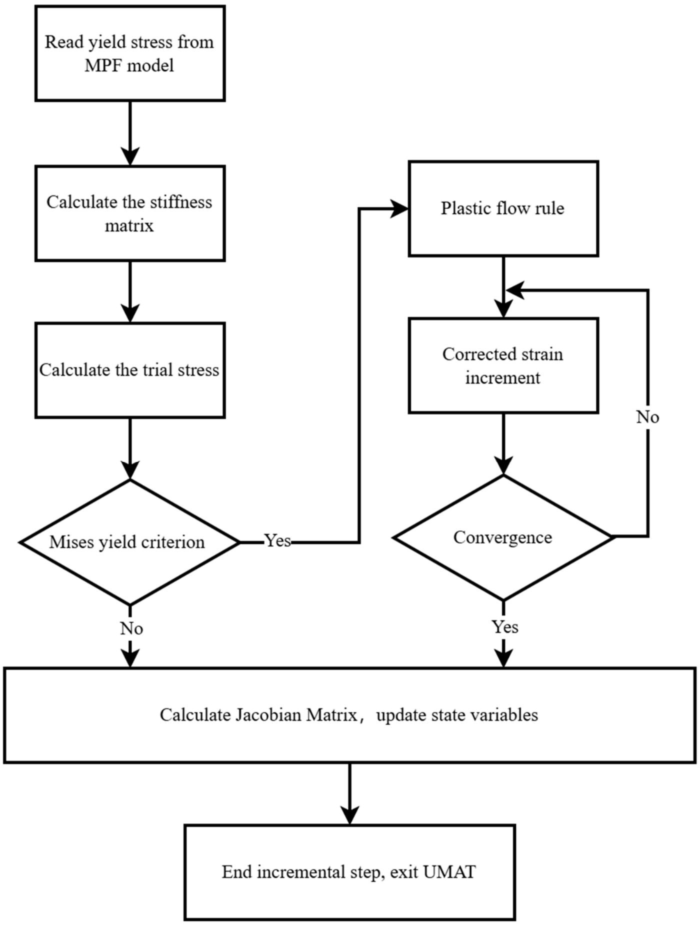

Figure 1. Flowchart of UMAT subroutine.

The expression for the shear modulus is given by

$$\mu = \frac{E}{2(1+v)} \tag{10}$$

At the beginning of each incremental step, the elastic trial stress $\boldsymbol{\sigma}^{\mathrm{tr}}$ of the material is calculated using the elastic stiffness matrix $\mathbf{C}$ based on the given total strain increment $\Delta\varepsilon$, which is used to determine whether the material enters the plastic deformation region or not. The formula for calculating the elastic trial stress is given below:

$$\sigma^{\mathrm{tr}} = \boldsymbol{\sigma}_{\boldsymbol{t-1}} + \mathbf{C}\,\boldsymbol{\Delta\varepsilon} \tag{11}$$

where $\boldsymbol{\sigma}_{t-1}$ is the stress tensor at the last incremental step, and $\Delta\boldsymbol{\varepsilon}$ is the total strain increment.

To determine whether plastic deformation has occurred in the material, the equivalent trial stress, σ_e^{tr}, is calculated. According to the von Mises criterion, the equivalent trial stress is calculated as follows:

$$\sigma_e^{tr} = \sqrt{\frac{1}{2}\left[\left(\sigma_{11}^{tr}-\sigma_{22}^{tr}\right)^2 + \left(\sigma_{11}^{tr}-\sigma_{33}^{tr}\right)^2 + \left(\sigma_{22}^{tr}-\sigma_{33}^{tr}\right)^2 + 6\left(\sigma_{12}^{tr}\right)^2\right]} \tag{12}$$

If the equivalent trial stress exceeds the yield stress calculated from the MPF model, the material enters the plastic deformation region.

After confirming that plastic deformation has occurred, the plastic strain increment $\Delta\varepsilon_p$ is calculated. In this study, an iterative method is used to approximate the strain increment step by step to ensure the accuracy of the stress update. In each iteration, the error $r^{(i)}$ is defined as the difference between the equivalent trial stress and the yield stress:

$$r^{(i)} = \sigma_e^{tr} - 3\mu\Delta\varepsilon_p - \sigma_f \tag{13}$$

The updated expression for the incremental plastic strain is

$$\Delta\varepsilon_p = \Delta\varepsilon_p^{(i)} + \frac{r^{(i)}}{3\mu} \tag{14}$$

where $\Delta\varepsilon_p^{(i)}$ is the plastic strain increment in the current iteration step.

Once the equivalent strain increment is determined, the stress, elastic strain, and plastic strain tensors for the current increment step are updated using the following formulas:

$$\boldsymbol{\sigma} = \frac{\sigma_f}{\sigma_e^{\mathrm{tr}}}\,\boldsymbol{\sigma}^{tr} + \boldsymbol{\delta}\,\sigma_h \tag{15}$$

$$\boldsymbol{\varepsilon}^p = \boldsymbol{\varepsilon}_{t-1}^p + \frac{3}{2}\Delta\varepsilon_p\,\frac{\boldsymbol{\sigma}^{tr}}{\sigma_e^{tr}} \tag{16}$$

$$\boldsymbol{\varepsilon}^e = \boldsymbol{\varepsilon} - \boldsymbol{\varepsilon}^p \tag{17}$$

where σ_h is the hydrostatic pressure, and δ is the Kronecker symbol, expressed in terms of the unit matrix.

2.3. Model Coupling

In this study, a multiscale model was developed to couple the macroscopic finite element method (FEM) with the microstructural evolution simulated by the multiphase field model (MPFM). The coupling schematic of the FEM and the MPFM is shown in Figure 2. The FEM calculates the macroscopic mechanical response, including plastic deformation, using the yield stress obtained from the MPFM. At each time increment, the yield stress required for the FEM is updated based on the microstructural state, which evolves according to the dynamic recrystallization process simulated by the MPFM. This exchange is facilitated by the UEXTERNALDB subroutine, which provides the updated yield stress from the MPFM to the UMAT subroutine within Abaqus. Figure 3 illustrates the flow of data, showing how the FEM calls the MPFM at each step to retrieve microstructure-informed yield stress values, ensuring that the macroscale deformation reflects ongoing microstructural changes.

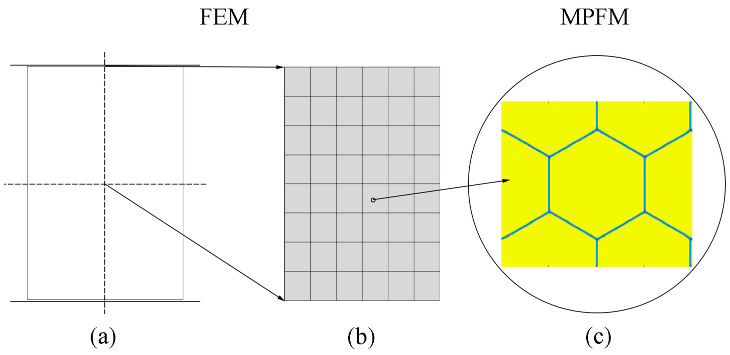

Figure 2. A schematic diagram of the coupling between the FEM and the MPFM: (**a**) the macroscopic bulk body; (**b**) discretization with finite elements; (**c**) the MPFM.

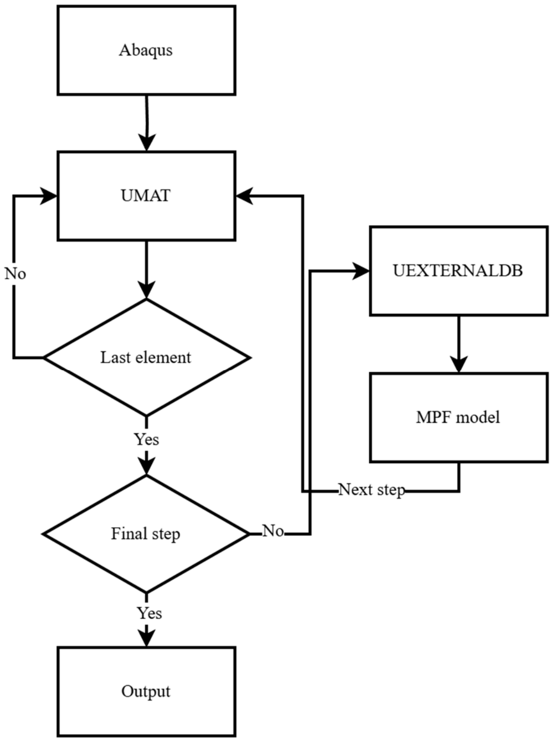

Figure 3. Flowchart of multiscale model.

In the coupled micro–macro field calculation, the time increment, Δt, is determined by satisfying the numerical stability conditions. When solving Equation (1) in two dimensions, the time increment Δt becomes $\Delta t = \Delta x^2/8\alpha^2 M^{\phi}$. The effective strain rate $\dot{\varepsilon}$ and temperature T of each element are transferred from the FEM to the MPFM. In the MPFM calculation, the dislocation density in the grains is calculated by substituting the effective strain rate $\dot{\varepsilon}$, temperature T, and effective strain increment $\Delta\varepsilon = \dot{\varepsilon}\Delta t$ into Equation (5). The critical dislocation density qc and the dynamic recrystallization (DRX) nucleation rate n_{DRX} also vary with $\dot{\varepsilon}$ and T. At the end of the MPFM, the yield stress σ_f is calculated using Equation (6) and passed back to the FEM.

The variables involved in the multiscale model calculations are stored and output as state variables (SDVs) in Abaqus. The significance of these state variables is detailed in Table 1. In this study, for a two-dimensional (2D) simulation, the elastic and plastic deformation tensors are represented with four components each, covering the in-plane components and an additional out-of-plane component (33 direction) to capture any effects related to plane stress or plane strain conditions. Although the primary deformation occurs within the 2D plane (11 and 22 directions), the 33-component is included to maintain consistency with Abaqus's plane strain or axisymmetric element formulations (such as CAX8 and CPE8). This approach allows us to monitor and store any out-of-plane strain or stress if it arises, even if it remains zero or constant under ideal 2D conditions.

Table 1. Significance of state variables.

SDVs	Significance
1~4	Elastic deformation tensor ($\varepsilon_{11}^{\mathrm{e}}, \varepsilon_{22}^{\mathrm{e}}, \varepsilon_{33}^{\mathrm{e}}, \varepsilon_{12}^{\mathrm{e}}$)
5~8	Plastic deformation tensor ($\varepsilon_{11}^{\mathrm{p}}, \varepsilon_{22}^{\mathrm{p}}, \varepsilon_{33}^{\mathrm{p}}, \varepsilon_{12}^{\mathrm{p}}$)
9	Equivalent strain
10	Equivalent strain increment
13	Dynamic recrystallization volume fraction
14	Grain size

3. Simulation Parameters and Conditions

3.1. Single-Element Hot Compression Simulation

The chemical composition of the materials used in this study is shown in Table 2. The parameters for the MPFM were derived from hot compression experiments, conducted under deformation temperatures of 950, 1000, 1050, 1100, and 1200 °C and strain rates of 0.001, 0.005, 0.01, 0.05, and 0.1 s^{-1}. Specifically, data at deformation temperatures of 1000, 1100, and 1200 °C with strain rates of 0.001, 0.01, and 0.1 s^{-1} were used to calibrate the model, while data from other conditions were reserved for validation purposes. Detailed methods for obtaining material parameters for the MPFM, including experimental setup, data processing, and parameter fitting, are provided in Supplementary Material. The resulting MPFM parameters used in this study are listed in Table 3.

Table 2. Chemical composition of experimental steel.

C	Si	Mn	Cr	Mo	Ni	Cu	P	S	Fe
0.39	0.24	0.72	1.12	0.189	0.09	0.01	0.012	0.004	bal

Table 3. MPFM parameters.

Parameter Name, Symbol	Parameter Value (Unit)
Grid size, Δx	1 (μm)
Grain boundary thickness, δ	3.5 (μm)
Grain boundary energy, γ	0.1 ($J \cdot m^{-2}$)
Dislocation interaction coefficient, α	0.5
Elastic modulus, E	$234.15 - 0.1015T$ (Gpa)
Poisson's ratio, v	$0.2756 + 0.00006T$
Burgers vector, b	0.258 (nm)
Nucleation rate formula constant, C	1.5994×10^4
Nucleation rate formula exponent, m	0.3902
Nucleation activation energy, Q_a	8830 ($J \cdot mol^{-1}$)
Interface mobility constant, M_0	1.402 ($m^4 \cdot K \cdot J^{-1} \cdot s^{-1}$)
Initial dislocation density, ρ_0	1×10^9 (m^{-2})
Peak stress, σ_p	$\sigma_p = 0.31(Z)^{0.1822} = 0.31\left(\dot{\varepsilon}exp\left(\frac{362{,}000}{RT}\right)\right)^{0.1822}$ (Mpa)
Initial stress, σ_0	$\sigma_0 = 0.52\sigma_p$ (MPa)
Critical stress, σ_c	$\sigma_c = 0.84\sigma_p$ (MPa)

To verify the accuracy of the multiscale model, a single-element hot compression multiscale model was developed using the Gleeble 3800 thermal simulation test machine (Dynamic Systems Inc., Buford, GA, USA) as a prototype. Due to symmetry, a quarter-model approach was adopted, as illustrated in Figure 4. The simulation parameters are provided in Table 4.

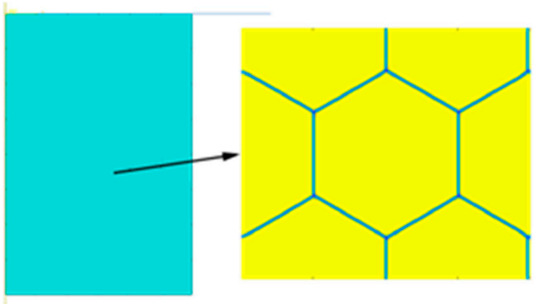

Figure 4. Multiscale model of single-element hot compression simulation.

Table 4. Single-element hot compression simulation parameters.

Parameters	Parameter Values (Unit)
Workpiece dimensions	5 × 7.5 (mm)
Friction coefficient	0
Strain rate	0.001, 0.005, 0.01, 0.05, 0.1 (s^{-1})
Deformation temperature	950, 1000, 1050, 1100, 1200 (°C)
Total strain	0.5
Mesh type	CAX8 (8 integration points)
Number of elements	1

3.2. Reduction Pretreatment (RP) Process

To simulate the RP process, a two-dimensional single-pass hot rolling model was developed using a two-roll mill as the prototype, as depicted in Figure 5. A microstructure field was defined within each element of the model. The effect of deformation temperature was investigated by simulating the RP process at billet surface temperatures of 900, 950, and 1000 °C. Temperature fields corresponding to these surface temperatures are shown in Figure 6 [37]. To examine the effect of reduction amount, the temperature field at a surface temperature of 950 °C (from Figure 5) was used to simulate the RP process with reduction ratios of 6.67, 13.3, and 20.0%. The simulation parameters are summarized in Table 5.

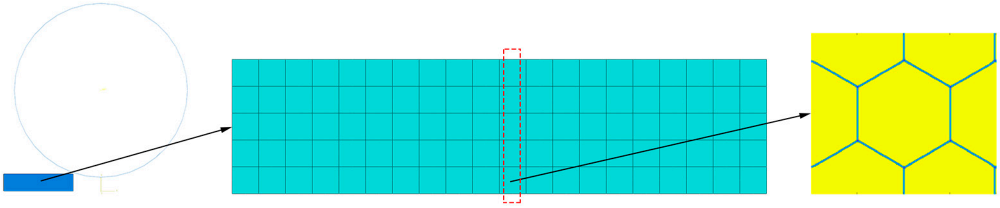

Figure 5. Multiscale model of RP process.

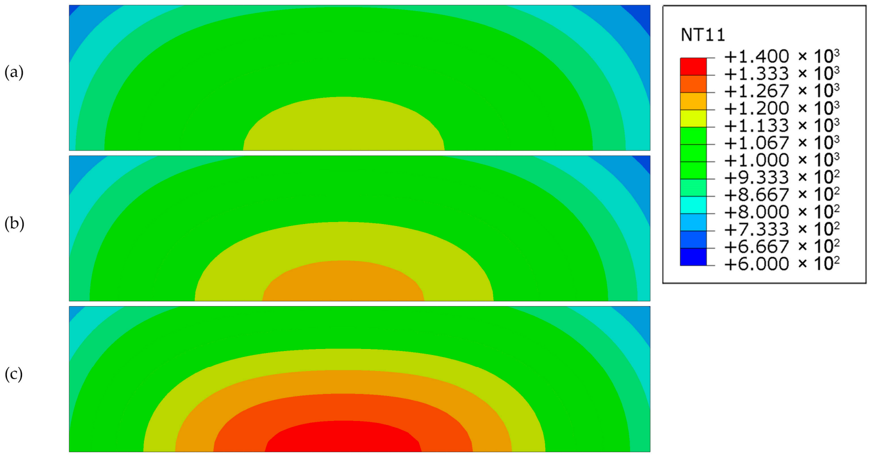

Figure 6. Temperature distribution in the billet at different billet surface temperatures: (**a**) 900 °C; (**b**) 950 °C; (**c**) 1000 °C.

Table 5. RP process simulation parameters.

Parameters	Parameter Value (Unit)
Roll diameter	750 (mm)
Workpiece dimensions	300 × 75 (mm)
Friction coefficient	0.2
Rolling speed	100 (mm/s)
Mesh type	CPE8
Number of elements	20 × 5

This study focused on dynamic recrystallization (DRX) during the reduction pretreatment (RP) process and, thus, did not include the static recrystallization or grain growth that might occur post deformation. This approach simplifies the simulation and is based on the assumption that dynamic recrystallization primarily occurs during active deformation. In particular, the MPFM calculations for a given cell are terminated when the plastic strain increment reaches zero, as illustrated in Figure 7. The appearance of a blue region in the figure represents a zero plastic strain increment, indicating that deformation in that cell has ceased. As subsequent microstructural evolution without active deformation is typically driven by static recrystallization and grain growth, which fall outside of the scope of dynamic recrystallization, the calculations for that cell are halted at this point. This assumption allows us to isolate the dynamic effects during deformation while reducing computational complexity.

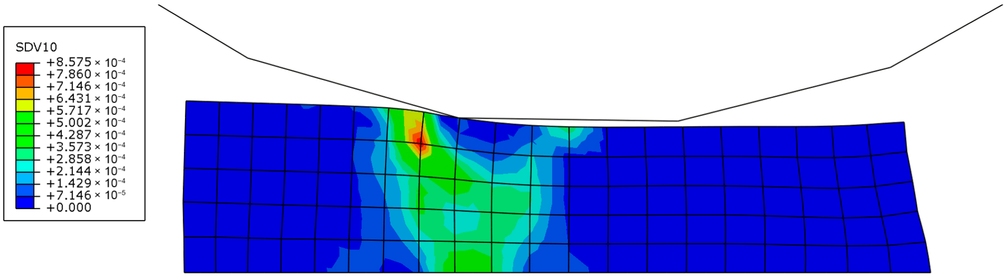

Figure 7. A schematic diagram of the conditions for stopping the MPFM calculation.

To quantitatively describe the deformation and dynamic recrystallization behavior during the RP process, the variations in plastic strain, dynamic recrystallization volume fraction, and grain size from the surface to the core of the billet, as highlighted in the red box in Figure 5, were statistically analyzed.

4. Results and Discussion

4.1. Single-Element Hot Compression Simulation

To validate the accuracy of the current model, a uniaxial compression test was simulated using a single element. A comparison between the simulated macroscopic stress and the experimental results is presented in Figure 8. The figure clearly shows that the dynamic recrystallization characteristics of the stress–strain curve are well captured, demonstrating that the multiscale model effectively simulates both work hardening and dynamic softening during material deformation. Furthermore, the multiscale model exhibits high predictive accuracy for both the modeling and validation datasets, indicating that the MPFM provides reliable stress predictions for simulating the hot deformation process.

Figure 9 illustrates the variation in the dynamic recrystallization volume fraction with strain under different conditions. The simulation results demonstrate a classic S-shaped trend in the kinetics of dynamic recrystallization. At a constant strain rate, the dynamic recrystallization volume fraction increases with temperature for the same strain, and the rate of complete recrystallization also accelerates. This behavior is influenced by two primary factors: the number of dynamic recrystallization nuclei and the growth rate of recrystallization grains. The number of nuclei depends on both the nucleation site density and the nucleation rate.

As indicated by Equations (3) and (6), both grain boundary mobility and nucleation rate increase with temperature at the same strain rate, leading to an accelerated rate of dynamic recrystallization. A comparison of the simulation and experimental results reveals that the simulation closely aligns with the experimental data at strain rates of 0.01 and 0.1 s^{-1}. However, at a strain rate of 0.001 s^{-1}, the simulation results at 1200 °C and 1100 °C deviate significantly from the experimental data. This discrepancy arises because dynamic recrystallization occurs multiple times during hot deformation under high-temperature and low-strain-rate conditions, causing the flow stress curve to exhibit a multi-peak pattern and leading to an inaccurate statistical representation of the dynamic recrystallization volume fraction.

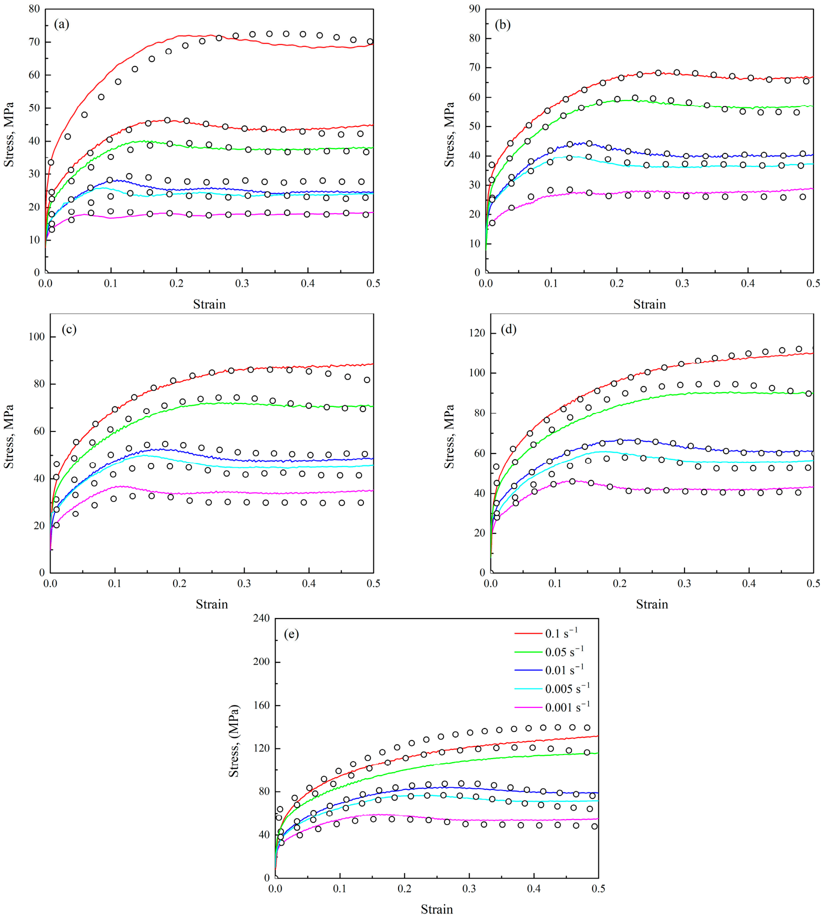

Figure 8. Comparison of experimental and simulated results of stress–strain curves (—: experimental results; ○: simulated results): (**a**) 1200 °C; (**b**) 1100 °C; (**c**) 1050 °C; (**d**) 1000 °C; (**e**) 950 °C.

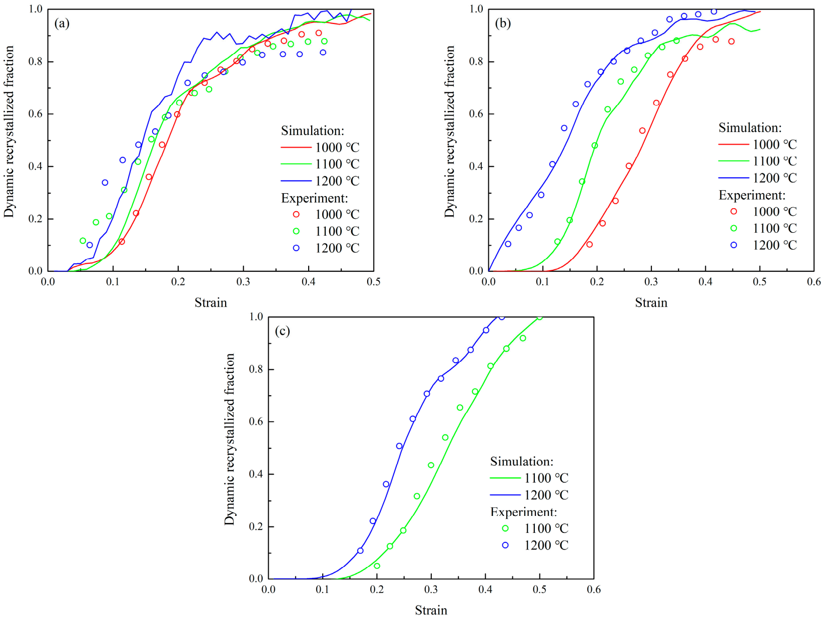

Figure 9. Variation in dynamic recrystallization volume fraction with strain: (**a**) 0.001 s^{-1}; (**b**) 0.01 s^{-1}; (**c**) 0.1 s^{-1}.

4.2. Effect of Reduction Amount

Figure 10 shows the effect of reduction amount on the plastic strain distribution in the billet during the RP process. At a small reduction ratio (6.67%), plastic strain is predominantly concentrated in the outer quarter of the billet. As the reduction ratio increases, the plastic strain progressively reaches the core and becomes more uniform. Figure 11 illustrates the variation in the plastic strain from the billet surface to the core. It is evident that, with an increasing reduction ratio, the plastic strain in the core of the billet rises significantly from 0.087 to 0.282.

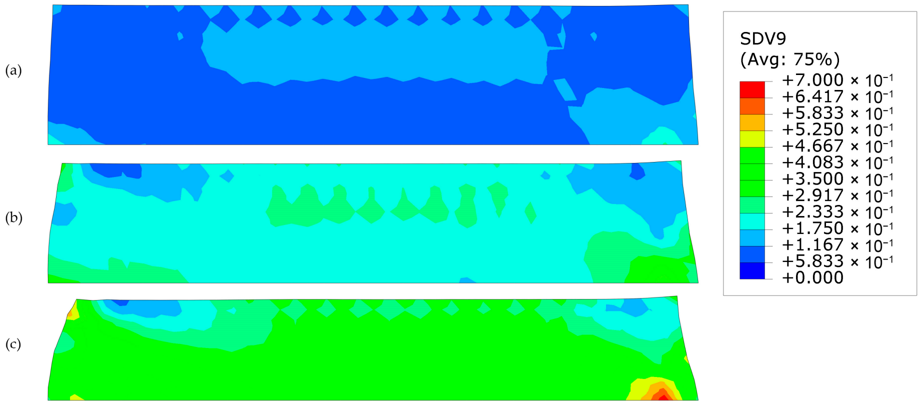

Figure 10. Distribution of plastic strain in billet under different reduction ratios: (**a**) 6.67%; (**b**) 13.3%; (**c**) 20.0%.

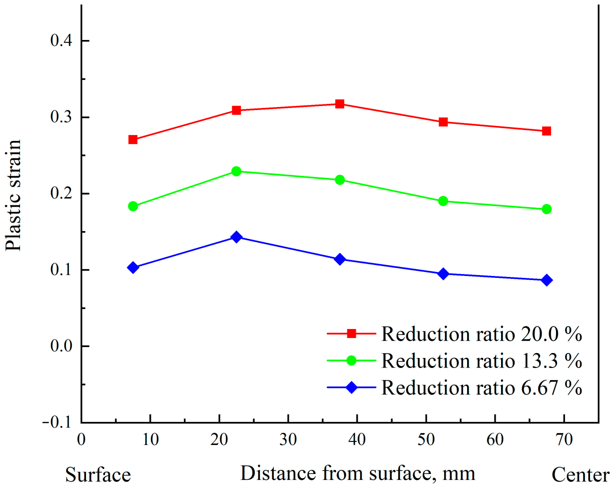

Figure 11. Variation in plastic strain with position under different reduction ratios.

Figures 12–15 illustrate the effect of the reduction ratio on the dynamic recrystallization behavior of the billet during the RP process. As the reduction ratio increases, the dynamic recrystallization volume fraction within the billet rises significantly, while the grain size decreases notably. Specifically, as the reduction ratio increases from 6.67% to 20.0%, the dynamic recrystallization volume fraction in the slab core increases from 0.009 to 0.682, and the grain size decreases from 121 µm to 67 µm, leading to a significant refinement of the billet core microstructure.

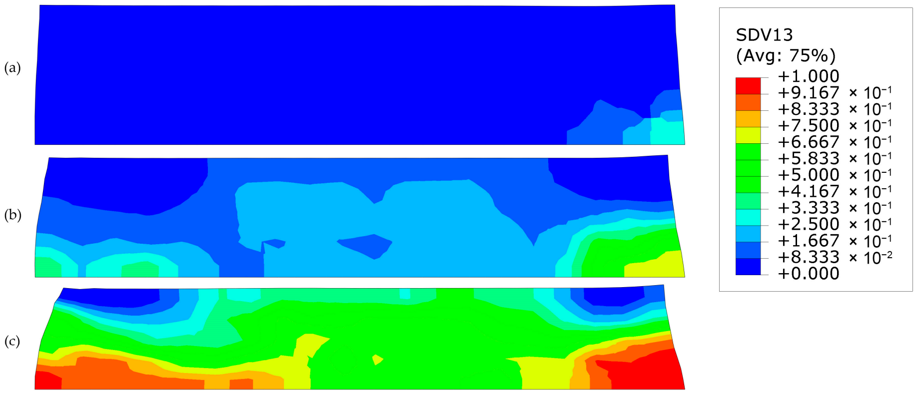

Figure 12. Distribution of dynamic recrystallization volume fraction in billet under different reduction ratios: (**a**) 6.67%; (**b**) 13.3%; (**c**) 20.0%.

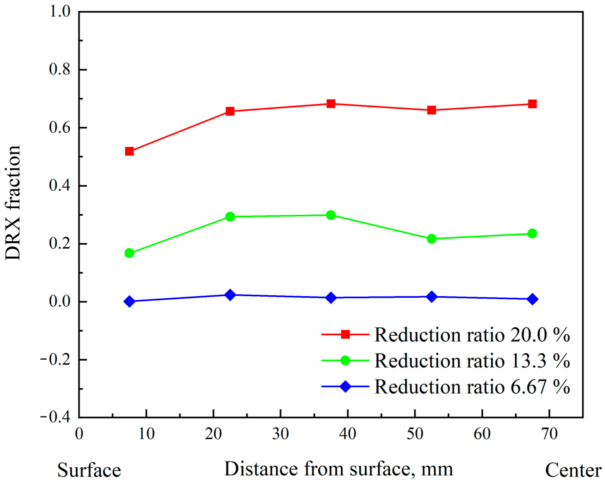

Figure 13. Variation in dynamic recrystallization volume fraction with position under different reduction ratios.

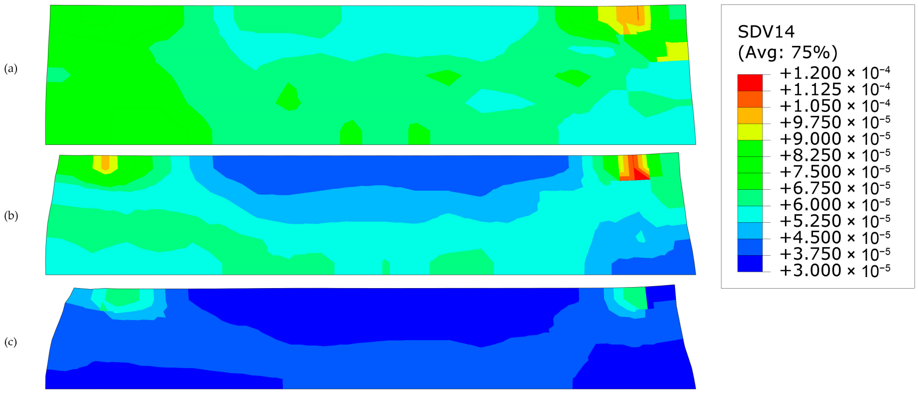

Figure 14. Distribution of grain size in billet under different reduction ratios: (**a**) 6.67%; (**b**) 13.3%; (**c**) 20.0%.

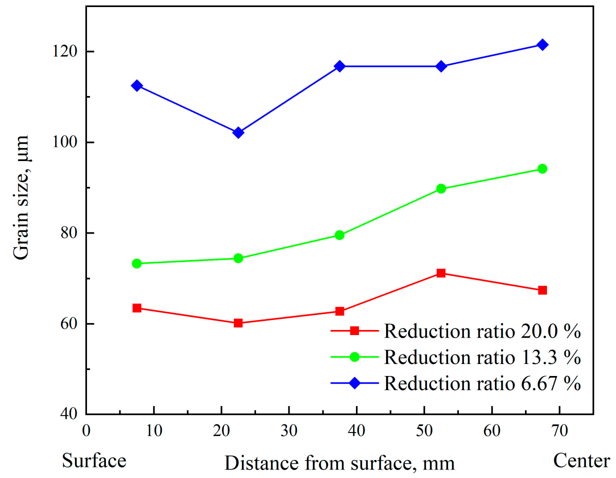

Figure 15. Variation in grain size with position under different reduction ratios.

4.3. Effect of Billet Surface Temperature

Figures 16 and 17 illustrate the effect of billet surface temperature on the internal plastic strain of the billet during the RP process. Figure 15 demonstrates that, as the billet surface temperature increases, the location of the maximum plastic strain shifts towards the core, and the plastic strain in the core rises. Specifically, when the billet surface temperature increases from 900 °C to 1000 °C, the plastic strain in the core increases from 0.173 to 0.183. Figure 16 further indicates that as the billet surface temperature increases, the difference between the plastic strain in the core and the maximum strain within the billet decreases from 0.062 to 0.042. This reduction suggests that higher surface temperatures during the RP process enhance the uniformity of internal deformation in the billet.

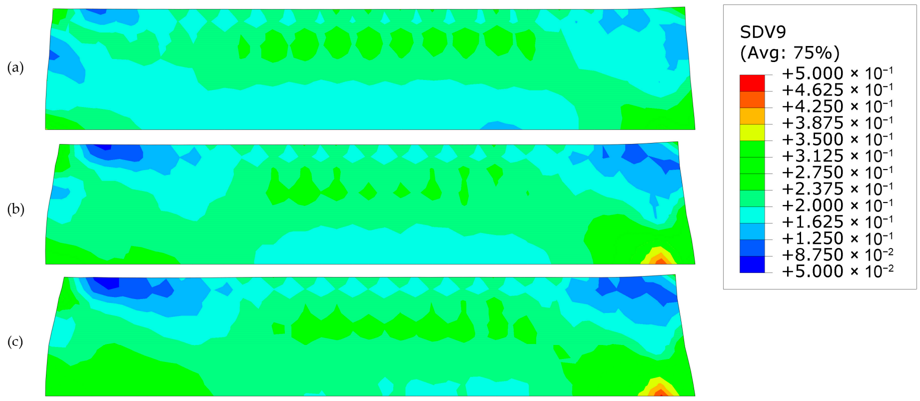

Figure 16. Distribution of plastic strain in billet under different billet surface temperatures: (**a**) 900 °C; (**b**) 950 °C; (**c**) 1000 °C.

Figures 18–21 illustrate the effect of billet surface temperature on the dynamic recrystallization behavior within the billet. As the surface temperature increases, the dynamic recrystallization volume fraction also rises. Specifically, when the billet surface temperature is increased from 900 °C to 1000 °C, the dynamic recrystallization volume fraction in the core rises from 0.029 to 0.36, as shown in Figure 18. At surface temperatures of 900 °C and 950 °C, the dynamic recrystallization volume fraction within the billet is relatively low. Consequently, the nucleation of dynamic recrystallization increases the number of grains and reduces the average grain size. However, despite this reduction in grain size, the overall trend shows that grain size generally increases with higher deformation temperature, as illustrated in Figure 20.

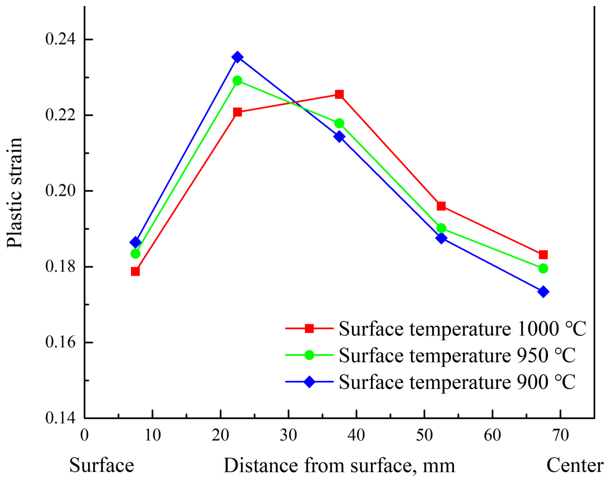

Figure 17. Variation in plastic strain with position under different billet surface temperatures.

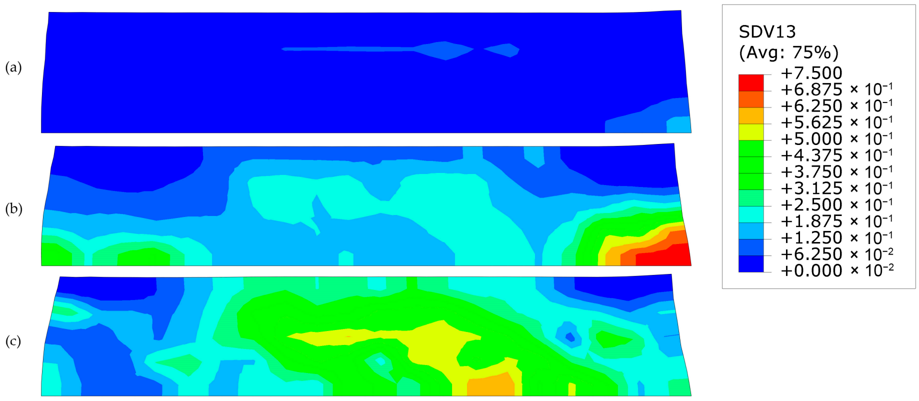

Figure 18. Distribution of dynamic recrystallization volume fraction in billet under different billet surface temperatures: (**a**) 900 °C; (**b**) 950 °C; (**c**) 1000 °C.

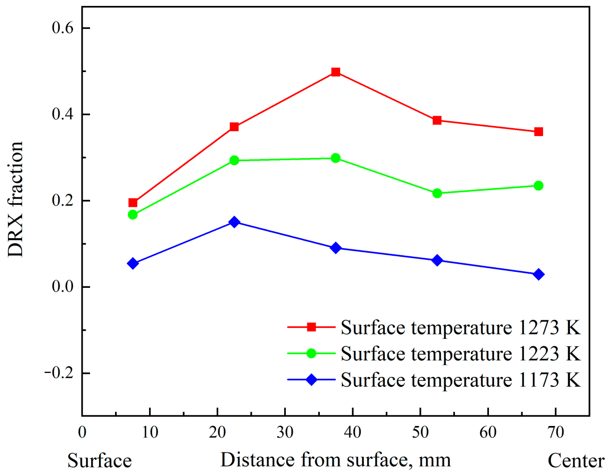

Figure 19. Variation in dynamic recrystallization volume fraction with position under different billet surface temperatures.

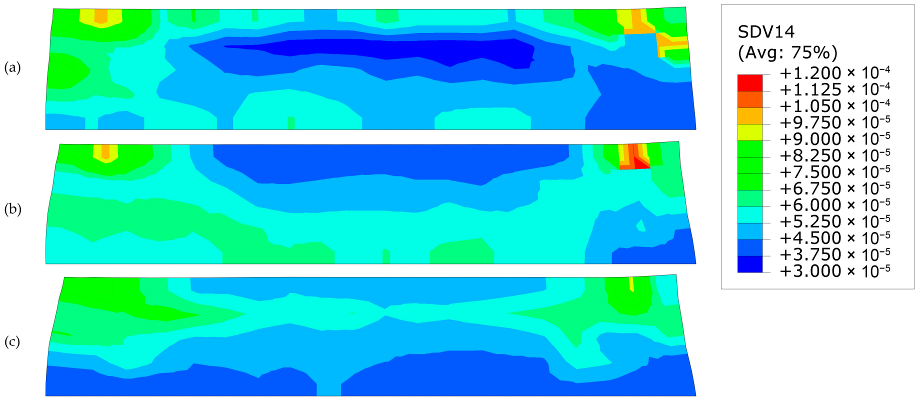

Figure 20. Distribution of dynamic recrystallization grain size in billet under different billet surface temperatures: (**a**) 900 °C; (**b**) 950 °C; (**c**) 1000 °C.

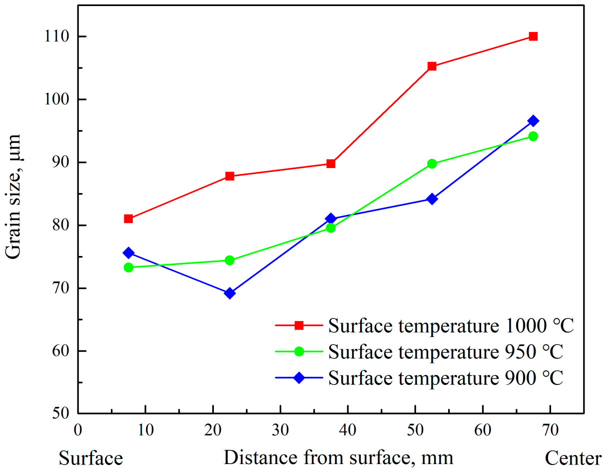

Figure 21. Variation in grain size with position under different billet surface temperatures.

In summary, both the reduction amount and billet surface temperature significantly impact the macroscopic mechanical behavior and microstructural evolution during the RP process. Increasing the reduction amount and billet surface temperature enhances the plastic strain and the dynamic recrystallization volume fraction in the core of the slab. These changes contribute to the closure of core voids and the refinement of the core's microstructure.

5. Conclusions

1. In this study, we successfully developed a multiscale model that couples the finite element method (FEM) with the multiphase field model (MPFM) through secondary development within Abaqus. The model accurately describes both macroscopic mechanical behavior and microstructural evolution during hot deformation, exhibiting high predictive accuracy, especially in simulations of dynamic recrystallization (DRX).
2. The findings reveal that, under the same billet surface temperature, increasing the reduction ratio significantly enhances the plastic strain and dynamic recrystallization volume fraction while concurrently reducing the grain size. When the reduction ratio is increased from 6.67% to 20.0%, the DRX volume fraction at the billet core rises from 0.009 to 0.682, while the grain size decreases from 121 μm to 67 μm.
3. Under the same reduction ratio, increasing the billet surface temperature enhances both the plastic strain and dynamic recrystallization volume fraction in the billet core. Specifically, when the billet surface temperature increases from 900 °C to 1000 °C, the dynamic recrystallization volume fraction in the core rises from 0.029 to 0.36, and the plastic strain increases from 0.173 to 0.183.

Supplementary Materials: The following supporting information can be downloaded at: https://www.mdpi.com/article/10.3390/met14111290/s1, Table S1: Chemical composition of experimental steel; Figure S1: Thermal compression process route; Figure S2: Stress-strain curves at different temperatures: (a) 1473 K; (b) 1373 K; (c) 1323 K; (d) 1273 K; (e) 1223 K; Figure S3: Diagram of Characteristic Stress Acquisition: (a) 7th-order Polynomial Fitting of Flow Stress Curve; (b) Stress-Work Hardening Rate Curve; Figure S4: Calculation process for parameter n and activation energy of deformation Q_{act}; Figure S5: Relationship between peak stress and other characteristic stresses: (a) initial stress and steady-state stress; (b) critical stress and saturation stress; Figure S6: Schematic diagram for calculating the volume fraction of dynamic recrystallisation; Figure S7: Variation of nucleation rate with temperature and strain rate: (a) temperature; (b) strain rate. References [35,36,38–43] are cited in the supplementary materials.

Author Contributions: Conceptualization, D.W. and W.Y.; methodology, D.W.; data curation, Z.N.; formal analysis, Z.N. and Y.Z.; investigation, Z.N.; resources, Y.Z.; writing—original draft preparation, D.W.; writing—review and editing, W.Y.; visualization, Y.Z.; validation, W.Y.; supervision, W.Y.; project administration, W.Y.; funding acquisition, W.Y. All authors have read and agreed to the published version of the manuscript.

Funding: This research received no external funding.

Data Availability Statement: The original contributions presented in this study are included in the article/Supplementary Materials. Further inquiries can be directed to the corresponding author.

Conflicts of Interest: Authors Die Wu, Zhen Ning, Yanlin Zhu were employed by the company Chengdu Advanced Metal Materials Industry Technology Research Institute Co., Ltd. The remaining author declare that the research was conducted in the absence of any commercial or financial relationships that could be construed as a potential conflict of interest.

References

1. Li, G.; Yu, W.; Cai, Q. Investigation of reduction pretreatment process for continuous casting. *J. Mater. Process. Technol.* **2016**, *227*, 41–48. [CrossRef]
2. Wang, Y.; Cai, Q.; Li, G.; Yu, W. Effects of Reduction Pretreatment on the Internal Quality of Casting Billets. *Steel Res. Int.* **2017**, *88*, 1600337. [CrossRef]
3. Li, H.; Li, T.; Li, R.; Gong, M.; Wang, Z.; Wang, G. Effect of a Novel Hot-core Heavy Reduction Rolling Process after Complete Solidification on Deformation and Microstructure of Casting Steel. *ISIJ Int.* **2019**, *59*, 2283–22930. [CrossRef]
4. Li, T.; Li, H.; Li, R.; Wang, Z.; Wang, G. Work Roll Surface Profile Design and Optimization for Hot-core Heavy Reduction Rolling Process. *ISIJ Int.* **2019**, *59*, 1314–1322. [CrossRef]
5. Li, T.; Li, H.; Li, R.; Wang, Z.; Wang, G. Analysis of ductile fractures at the surface of continuous casting steel during hot-core heavy reduction rolling. *J. Mater. Process. Technol.* **2020**, *283*, 116713. [CrossRef]
6. Cheng, Z.; Liu, H.; Liu, Y.; Ning, Z.; Li, M.; Yu, W.; Cai, Q. Effects of Deformation Penetration and Recrystallization on the Internal Quality of Casting Ingot. *Steel Res. Int.* **2024**, *95*, 2300422. [CrossRef]
7. Cheng, Z.; Jiang, A.; Yu, W. Effects of Gradient Temperature Field on the Internal Quality of Casting Ingot. *Metall. Mater. Trans. B* **2024**, 1–11. [CrossRef]
8. Li, H.; Gong, M.; Li, T.; Wang, Z.; Wang, G. Effects of hot-core heavy reduction rolling during continuous casting on microstructures and mechanical properties of hot-rolled plates. *J. Mater. Process. Technol.* **2020**, *283*, 116708. [CrossRef]
9. Li, R.; Li, H.; Wang, L.; Wang, G.; Li, J.; Li, J. Influence of hot-core heavy reduction rolling on microstructure uniformity of casting billet. *Ironmak. Steelmak.* **2022**, *50*, 273–285. [CrossRef]
10. Naghdy, S.; Akbarzadeh, A. Characterization of dynamic recrystallization parameters for a low carbon resulfurized free-cutting steel. *Mater. Des.* **2014**, *53*, 910–914. [CrossRef]
11. Momeni, A.; Dehghani, K. Characterization of hot deformation behavior of 410 martensitic stainless steel using constitutive equations and processing maps. *Mater. Sci. Eng. A-Struct.* **2010**, *527*, 5467–5473. [CrossRef]
12. He, X.; Yu, Z.; Lai, X. A method to predict flow stress considering dynamic recrystallization during hot deformation. *Comput. Mater. Sci.* **2008**, *44*, 760–764. [CrossRef]
13. Wu, B.; Li, M.Q.; Ma, D.W. The flow behavior and constitutive equations in isothermal compression of 7050 aluminum alloy. *Mater. Sci. Eng. A-Struct.* **2012**, *542*, 79–87. [CrossRef]
14. Ji, H.; Liu, J.; Wang, B.; Tang, X.; Lin, J.; Huo, Y. Microstructure evolution and constitutive equations for the high-temperature deformation of 5Cr21Mn9Ni4N heat-resistant steel. *J. Alloys Compd.* **2017**, *693*, 674–687. [CrossRef]
15. Saadatkia, S.; Mirzadeh, H.; Cabrera, J. Hot deformation behavior, dynamic recrystallization, and physically-based constitutive modeling of plain carbon steels. *Mater. Sci. Eng. A-Struct.* **2015**, *636*, 196–202. [CrossRef]

16. Bharath, K.; Khanra, A.K.; Davidson, M.J. Hot deformation behavior and dynamic recrystallization constitutive modeling of Al–Cu–Mg powder compacts processed by extrusion at elevated temperatures. *Proc. Inst. Mech. Eng. Part L J. Mater.* **2021**, *235*, 581–596. [CrossRef]
17. Zheng, Y.; Liu, J.; Liang, Y.; Wu, P. Monte-Carlo-assisted phase field simulations of grain structure evolution during the welding process. *Metals* **2023**, *13*, 623. [CrossRef]
18. Wermiński, M.; Perzyński, K.; Sitko, M.; Madej, L. Evaluation of data transfer influence in coupled Monte Carlo finite element model on microstructure evolution predictions. *Mater. Res. Proc.* **2023**, *28*, 1551–1558.
19. Yu, P.; Wu, C.; Shi, L. Analysis and characterization of dynamic recrystallization and grain structure evolution in friction stir welding of aluminum plates. *Acta Mater.* **2021**, *207*, 116692. [CrossRef]
20. Svyetlichnyy, D. Frontal cellular automata for modelling microstructure evolution: Computational complexity analysis. *Comput. Mater. Sci.* **2023**, *230*, 112478. [CrossRef]
21. Łach, Ł. Modeling of Microstructure Evolution during Deformation Processes by Cellular Automata—Boundary Conditions and Space Reorganization Aspects. *Materials* **2021**, *14*, 1377. [CrossRef] [PubMed]
22. Sitko, M.; Banaś, K.; Madej, L. Scaling scientific cellular automata microstructure evolution model of static recrystallization toward practical industrial calculations. *Materials* **2021**, *14*, 4082. [CrossRef] [PubMed]
23. Liu, L.; Wu, Y.; Ahmad, A.S. A novel simulation of continuous dynamic recrystallization process for 2219 aluminium alloy using cellular automata technique. *Mater. Sci. Eng. A-Struct.* **2021**, *815*, 141256. [CrossRef]
24. Takaki, T.; Hisakuni, Y.; Hirouchi, T.; Yamanaka, A.; Tomita, Y. Multi-phase-field simulations for dynamic recrystallization. *Comput. Mater. Sci.* **2009**, *45*, 881–888. [CrossRef]
25. Takaki, T.; Yamanaka, A.; Tomita, Y. *Phase-Field Modeling for Dynamic Recrystallization*; Springer International Publishing: Berlin/Heidelberg, Germany, 2015.
26. Lyu, X.; Tian, C.; Shi, L.; Wu, C.; Chen, J.; Yu, P. Multi-scale modelling of the microstructure evolution during friction stir welding of 2195 Al–Li alloy. *J. Mater. Res. Technol.* **2024**, *28*, 1318–1329. [CrossRef]
27. Wang, J.; Chen, G.; Huang, S.; Zhang, H.; Chen, Q.; Zhang, C.; Du, Z. Multi-scale modeling and simulation for multi-pass processing of Ta-2.5 W alloy. *Int. J. Mech. Sci.* **2022**, *218*, 107069. [CrossRef]
28. Won Lee, H.; Im, Y. Numerical modeling of dynamic recrystallization during nonisothermal hot compression by cellular automata and finite element analysis. *Int. J. Mech. Sci.* **2010**, *52*, 1277–1289. [CrossRef]
29. Shabaniverki, S.; Serajzadeh, S. Simulation of softening kinetics and microstructural events in aluminum alloy subjected to single and multi-pass rolling operations. *Appl. Math. Model.* **2016**, *40*, 7571–7582. [CrossRef]
30. Lin, X.; Zou, X.; An, D.; Krakauer, B.W.; Zhu, M. Multi-Scale Modeling of Microstructure Evolution during Multi-Pass Hot-Rolling and Cooling Process. *Materials* **2021**, *14*, 2947. [CrossRef]
31. Xu, X.; Zhang, J.; Outeiro, J.; Xu, B.; Zhao, W. Multiscale simulation of grain refinement induced by dynamic recrystallization of Ti6Al4V alloy during high speed machining. *J. Mater. Process. Technol.* **2020**, *286*, 116834. [CrossRef]
32. Chen, F.; Zhu, H.; Chen, W.; Ou, H.; Cui, Z. Multiscale modeling of discontinuous dynamic recrystallization during hot working by coupling multilevel cellular automaton and finite element method. *Int. J. Plast.* **2021**, *145*, 103064. [CrossRef]
33. Takaki, T.; Yoshimoto, C.; Yamanaka, A.; Tomita, Y. Multiscale modeling of hot-working with dynamic recrystallization by coupling microstructure evolution and macroscopic mechanical behavior. *Int. J. Plast.* **2014**, *52*, 105–116. [CrossRef]
34. Yoshimoto, C.; Takaki, T. Multiscale hot-working simulations using multi-phase-field and finite element dynamic recrystallization model. *ISIJ Int.* **2014**, *54*, 452–459. [CrossRef]
35. Peczak, P.; Luton, M.J. The effect of nucleation models on dynamic recrystallization II. Heterogeneous stored-energy distribution. *Philos. Mag. B* **1993**, *68*, 115–144. [CrossRef]
36. Huang, K.; Logé, R.E. A review of dynamic recrystallization phenomena in metallic materials. *Mater. Des.* **2016**, *111*, 548–574. [CrossRef]
37. Ning, Z.; Yu, W.; Liu, H.Q.; Cai, Q.W. Effect of reduction pretreatment process on evolution of micro-porosity in 42CrMo billet. *J. Iron Steel Res. Int.* **2020**, *28*, 413–423. [CrossRef]
38. Jonas, J.J.; Quelennec, X.; Jiang, L.; Martin, É. The Avrami kinetics of dynamic recrystallization. *Acta Mater.* **2009**, *57*, 2748–2756. [CrossRef]
39. Kocks, U.F. Laws for Work-Hardening and Low-Temperature Creep. *J. Eng. Mater. Technol.* **1976**, *98*, 76–85. [CrossRef]
40. Mecking, H.; Kocks, U.F. A Mechanism for Static and Dynamic Recovery. In Proceedings of the 5th International Conference, Aachen, Germany, 27–31 August 1979; pp. 345–350.
41. Mecking, H.; Kocks, U.F. Kinetics of Flow and Strain-Hardening. *Acta Metall.* **1981**, *29*, 1865–1875. [CrossRef]
42. Derby, B. The dependence of grain size on stress during dynamic recrystallisation. *Acta Metall. Mater.* **1991**, *39*, 955–962. [CrossRef]
43. Derby, B. Dynamic recrystallisation: The steady state grain size. *Scr. Metall. Mater.* **1992**, *27*, 1581–1585. [CrossRef]